Ordering effect of kinetic energy on dynamic deformation of brittle solids

S. Mastilovic [a,*], A. Rinaldi [b], D. Krajcinovic [b]

[a] *Center for Multidisciplinary Studies, University of Belgrade*
Kneza Viseslava 1a, 11030 Belgrade, Serbia and Montenegro
[b] *Mechanical and Aerospace Engineering*
Arizona State University, Tempe, AZ 85287-6106

Abstract

The present study focuses on the plane strain problem of medium-to-high strain-rate loading of an idealized brittle material with random microstructure. The material is represented by an ensemble of "continuum particles" forming a two-dimensional geometrically and structurally disordered lattice. Performing repeated lattice simulations for different physical realizations of the microstructural statistics offers possibility to investigate universal trends in which the disorder and loading rate influence mechanical behavior of the material. The dynamic simulations of the homogeneous uniaxial tension test are performed under practically identical inplane conditions although they span nine decades of strain rate. The results indicate that the increase of the dynamic strength with the loading-power increase is also accompanied with a significant reduction of the strength dispersion. At the same time increase in the loading rate results in transition from random to deterministic damage evolution patterns. This ordering effect of kinetic energy is attributed to the diminishing flaw sensitivity of brittle materials with the

---

* Corresponding author. Tel.: +381 11 208 5059; fax: +381 11 305 5289.
E-mail address: gmvv@eunet.yu.

loading-rate increase. The uniformity of damage evolution patterns indicates an absence of the cooperative phenomena in the upper strain-rate range, in opposition to the coalescence of microcracks into microcrack clouds, which may represent the dominant toughening mechanism in brittle materials not susceptible to dislocation activities.

Keywords: Brittle solids; Dynamic tensile strength; Damage patterns; Ordering effect; Microcrack clouds

1. Introduction

The practical and scientific significance of deformation processes evolving at high strain rates is exceeded only by their complexity; the considered thermodynamic processes are non-stationary, non-local, and far from equilibrium. Despite the truly enormous progress in experimental analysis, there are inherent difficulties, if not limitations, when it comes to extreme loading rates ($\geq 10^7\ s^{-1}$). It is especially difficult to characterize the damage evolution and failure mechanisms due to the difficulty in recovering tested samples. The numerical experiments presented in this study cover the strain-rate range from medium to high, which are commonly explored by the Hopkinson bar and plate-impact experiments. The former is performed (up to $10^3 \div 10^4\ s^{-1}$) under uniaxial stress conditions while the latter (up to $10^7\ s^{-1}$) under uniaxial strain conditions. The objective of this investigation is to elucidate the effect of material micro-texture on fracture of dynamically-loaded brittle materials. The numerical simulations of the uniaxial tension test, the most common of all mechanical tests for structural materials, appear to be a useful tool for extrapolation of the experimental results.

The idealized brittle material is approximated by a two-dimensional triangular lattice: a Delaunay simplical graph dual to the irregular honeycomb system of Voronoi polyhedra representing, for example, grains of a ceramic material (Krajcinovic, 1996).[1] Grain boundaries, the most common examples of weak interfaces in brittle materials, are known to have a profound effect on their structure-sensitive properties such as the dynamic

[1] For a detailed discussion of the Voronoi tessellation, see, for example, Espinosa and Zavattieri, 2003, and references therein.

strength. The primary mechanism of damage evolution in polycrystalline ceramic materials is widely reported to be the intergranular microcracking. According to Lawn (1993), grain boundaries "are especially weak in ceramics because of the stringent directionality and charge requirements of covalent-ionic bonds." Furthermore, as the regions of lower atomic density, grain boundaries act as sources of, and sinks for, structural defects. Finally, sintering and hot pressing at high temperatures followed by cooling causes residual stresses due to the anisotropy of grains (Davidge and Green, 1968; Curtin and Scher, 1990). Therefore, in the present lattice model, the microstructural texture is represented by a network of grain boundaries; the cracking is assumed to be intergranular; and the local stress and strain fluctuations on a scale shorter than the grain facet size are neglected (Krajcinovic, 1996). In more general terms, we may think of lattice models as "a discretization of higher than one-dimensional materials by a network of one-dimensional elements characterized by element constitutive equations, and a breaking condition," (Jagota and Bennison, 1994). The model incorporates both variability and uncertainty in a straightforward manner. Variability, also termed randomness or aleatory variability, is the natural randomness in the process. Uncertainty, also termed epistemic uncertainty, is the uncertainty in the model; it is due to limited knowledge or limited availability of data or both. The mesoscale material texture is an example of the aleatory variability. The disorder may be topological (unequal coordination number), geometrical (unequal length of bonds), or structural (unequal strength and stiffness of bonds). The disorder is further enhanced by damage evolution, which is governed (to an extent depending on the deformation rate) by the local

fluctuations of the energy barriers quenched within the material, and the local fluctuations of stress.

Finally, although the lattice models are used often in modeling the fracture behavior of inhomogeneous or multi-phase systems, it is important to recognize their deficiencies and limits of their applicability. The two-dimensional systems exhibit inherent topological limitations; and the extreme geometrical disorder, which is intentionally used in this study, causes additional side effects. Nonetheless, we believe that the most notable numerical artifacts of lattice models (Jagota and Bennison,1994; Monette and Anderson, 1994) do not have a first-order effect on universal trends observed in this investigation, keeping in mind that we are dealing with relatively large geometrical and structural disorder and the nucleation-dominated damage evolution modes.

2. Details of the simulation

The approximation of a material by a particle lattice is inspired by the mesoscale morphology of a certain class of brittle materials, and successes of molecular dynamics method as a tool of solid mechanics (for overview of molecular dynamics, see, for example, Hoover, 1986; and Allen and Tildesley, 1994). Within this framework, continuum can be defined as a collection of discrete elements, known as "continuum particles" (Wiener, 1983). Assuming that positions and momenta of particles are known in the reference state, determination of all subsequent states is a problem of Hamiltonian mechanics. A number of numerical techniques are available to accomplish this task, including the most widely used the Verlet, Störmer, and Gear predictor-corrector

algorithms. The choice of the solution technique is largely a matter of preference since all of these methods are stable as long as the time step is carefully selected (Allen and Tildesley, 1994).

Since the lattice model used in this study is described in detail elsewhere (Mastilovic and Krajcinovic, 1999, 1999a) only a brief summary is presented herein. The average distance between two neighboring particles ($\bar{\lambda}$) is the model resolution length (l_c). (Hence, the effect of all defects smaller than the resolution length and the residual stress along the grain boundary must be introduced through the strength distribution.) The particles located in lattice nodes interact through the central force links with their nearest neighbors. The properties of these bonds are approximated by a nonlinear force-elongation relation (the Hook potential in tension and the Born-Meyer inspired potential in compression).

The size of grains and strength of grain boundaries are stochastic parameters in polycrystalline ceramic materials. Consequently, the lattice morphology is random as well; it is defined by the coordination number z and link length λ. In the pristine state, all lattices used in this study are topologically ordered by selecting $z = 6$ for all bulk-particles. The lattices are geometrically disordered since the equilibrium distances between particles (initial link lengths $\equiv \lambda_0$) are sampled from the normal distribution within the range $\alpha\ \bar{\lambda} \le \lambda \le (2-\alpha)\,\bar{\lambda}$. The geometrical-order parameter α, $(0 \le \alpha \le 1)$, is the model parameter that defines bandwidth of the geometrical disorder of the material (for example, the distribution of grain sizes). The lattice is also structurally disordered. The link stiffnesses are uniformly distributed within the range $\beta\ \bar{k} \le k \le (2-\beta)\,\bar{k}$, where β, $(0 \le \beta \le 1)$, is the structural-order parameter defining the stiffness distribution,

which takes into account the inherent or induced flaw structure of the material (e.g., flaw types, flaw spacing, flaw size, etc.). The link-rupture criterion is defined in terms of the critical link elongation. That is, the link between particles *i* and *j* ruptures (as its force-carrying capacity in tension is permanently lost) when the link elongation reaches the critical value $\varepsilon_{ij} = \Delta\lambda_{ij} / \lambda_{0ij} = \varepsilon_{cr} = const.$.

The parameters recorded through the entire process are: the position and velocity of each particle, number of ruptured links, and force in each link. Calculation of the deformation and kinetic energy, knowing the position and velocity of each particle, is straightforward. The density of isotropic damage is defined by the fraction of broken bonds $D=n/N$, where n and N are the number of broken bonds and the total number of bonds, respectively. The statistical mechanics expressions for the components of the stress and effective stiffness tensors are adopted from the molecular dynamics (Vitek, 1996).

In the molecular dynamics, it is common practice for the systems consisting of just one type of molecule to set the mass of the molecule as a fundamental unit, and to use the reduced units in simulations. For the simple pair potentials, the relations between reduced and physical units are defined by analytical expressions (Allen and Tildesley, 1994). For the lattice simulations performed in this study, the conversion of the reduced units into the physical (SI) units is estimated in the following manner. Assuming that the brittle material of our choice is alumina (Al_2O_3) with average grain diameter $D = l_c = 10\,\mu m$ and velocity of elastic longitudinal wave propagation $C_L \approx 10\,km/s$ (Straβburger and Senf, 1995), the ratio $\Delta t/\Delta t^* = \left(l_c/l_c^*\right)\cdot\left(C_L^*/C_L\right) \approx 10^{-8}\,s$ between the time interval (Δt) in SI unit and corresponding non-dimensional time interval $\left(\Delta t^*\right)$ is defined in terms of

the physical (l_c, C_L) and non-dimensional $(l_c^* \equiv 1,\ C_L^* = 7.2)$ material properties. (The non-dimensional velocity of the elastic wave propagation is estimated from the simulation; see Fig. 2a.) The ratio $\dot{\varepsilon}/\dot{\varepsilon}^* = \Delta t^*/\Delta t \approx 10^8\ s^{-1}$ between the strain rate in *SI* unit and non-dimensional strain rate is inversely proportional to the corresponding time interval ratio.

The computer simulations of the homogeneous uniaxial tension test are conceptually very simple. The problem of the uniform distribution of load within a sample is solved by imposing an initial velocity field to the lattice at *t=0*. The velocity, $v_H = \pm \dot{\varepsilon}_y\ L/2$, at the top (+) and bottom (-) surface of the sample is defined in the terms of the prescribed strain rate, $\dot{\varepsilon}_y = \dot{L}/L$, where *L* is the length of the sample (Fig. 1a). A homogeneous velocity gradient is imposed to all other particles in the loading direction according to the linear form $\dot{y} = \dot{\varepsilon}_y\ y$. Subsequently, only the velocity of the particles located at the boundary is controlled, while the motion of the other particles is governed by equation of motion (Fig. 1b). A similar approach was used by Holian and Grady (1988) to simulate the homogeneous adiabatic expansion. The lateral inertia is overcome in a similar way, by applying a velocity $\dot{x} = \upsilon_0^{\varepsilon}\ \dot{\varepsilon}_y\ x$ to all particles in the lattice. The plane strain Poisson's ratio $\upsilon_0^{\varepsilon} = 1/3$, which is characteristic of the two-dimensional triangular lattice, corresponds to the Poisson's ratio $\upsilon_0 = 1/4$ of a pristine material.

The effectiveness of this loading procedure is illustrated by Figs. 2 and 3. In Fig. 2, the longitudinal stress (the normal stress in *y*-direction) is plotted vs. time for the displacement controlled test at the loading rate $\dot{\varepsilon} = 100\ s^{-1}$. The controlled displacement is applied at both the top and bottom surface of the model. The "local" stresses presented

in Fig. 2a are recorded at points P_1 and P_3 along the symmetry axis (Fig. 1b). The solid line represents the average ("global") strain in the sample. The curves representing the evolutions of the local stress are of the staircase form. Each step marks one complete wave transit through the sample. A qualitatively identical behavior is observed during the Hopkinson bar experiments (Nicholas and Bless, 1985). If only few wave transits occur before the specimen fails the stress state within the sample is not uniform and the volume averaging of the stress and strain is not appropriate. On the other hand, if, the previously described, velocity fields are imparted to the lattice at $t = 0$, the local values of both strain and strain rate are almost the same as the value obtained by averaging over the entire volume of the sample (Fig. 2b).

As a consequence of the initial velocity (strain rate) field applied perpendicular to the loading (y-) direction, the stress in the lateral (x-) direction is approximately zero regardless of the strain rate of the external load applied in longitudinal direction (Fig. 3).

It is worth emphasizing that simulations of the uniaxial tension test cannot be performed at all at high strain rates unless the initial velocity (strain rate) field is applied. The reason for this is that, in the present lattice model, the fracture criterion is defined in terms of a relatively small critical link extension $\varepsilon_{cr} = 0.1\%$; hence, at rapid loading rates the top- and bottom-boundary particles, to which the prescribed displacement is directly applied, separate from the rest of the lattice.

The 30 physical realizations are performed repeatedly at 5 different strain rates: 1 s^{-1}, 10 s^{-1}, 1×10^3 s^{-1}, 1×10^5 s^{-1}, 1×10^7 s^{-1}. For the reason of computational economy only a single realization is performed at other loading rates (see Fig. 5 for the complete list).

2.1. Lattice parameters

The uniaxial tension simulations are performed on the 192×227 lattice. This lattice size ensures the size-independency of the results, according to comparison of results obtained for four different lattices (288×339, 192×227, 96×115, 48×61).

The reduced-units geometric and structural parameters of the lattice are: the average (mean) link stiffness $\bar{k} = 50$, the structural-order parameter $\beta = 0.5$, the average equilibrium distance between particle sites $\bar{\lambda} = l_c = 1$, the geometrical-order parameter $\alpha = 0.02$, and the rupture strain of the links $\varepsilon_{cr} = 0.1\%$ (Mastilovic and Krajcinovic, 1999, 1999a).

The chosen value of the geometrical-order parameter ensures, within topological limitations of the model, reasonable similarity between the lattice texture and typical grain structures of ceramics (for example, Lawn, 1995; Sarva and Nemat-Nasser, 2001; Espinosa and Zavattieri, 2003). In hindsight, $\varepsilon_{cr} = 0.1\%$ proves to be an underestimate in combination with $\alpha = 0.02$ and $\beta = 0.5$, since it results in too small quasi-static macro-failure strain.

The size of the reduced-unit computational time step was investigated beforehand by Mastilovic and Krajcinovic (1999); it was estimated, again based on the molecular dynamics analogy, that the use of any time step equal to or smaller than $\delta t^* = 0.01$ leads to the stable and time-step-insensitive results. (Note that $\delta t^* = 0.01$ corresponds to the physical value of $\delta t = 0.01 \cdot 10^{-8}\ s = 100\ ps$.) It should be emphasized, though, that for the extremely high strain-rate simulations the "accuracy" of the strength estimate may

depend on the selected output frequency of the data collection, which is limited by the computational time step. This is not an issue for the medium strain-rate simulations where the time averaging is performed over a large number of computational cycles. Consequently, the medium strain-rate simulations, from 0.1 s^{-1} to 1×10^4 s^{-1}, are performed at the non-dimensional computational time step $\delta t^* = 0.01$ (100 ps); while $\delta t^* = 0.0001$ (1 ps) is used for the simulations within the strain-rate range [1×10^5 s^{-1}, 2×10^6 s^{-1}]. The two highest strain rate simulations (1×10^7 s^{-1} and 1×10^8 s^{-1}) are performed with $\delta t^* = 0.00001$ (0.1 ps).

3. Results

3.1 Dynamic tensile strength

The stress-strain curves obtained for 30 realizations at strain rates 1 s^{-1} and 1×10^7 s^{-1} are presented in Fig. 4. Three qualitative observations can be made:

- the response is nearly linear up to failure for moderate and the highest strain rates, but not for the transient strain rates characterized by the rapid strength increase,
- the loading-rate increase results in increase of the dynamic tensile strength (σ_m);
- the loading-rate increase results in decrease of the strength dispersion.

The maximum dynamic tensile strength is more than twice the minimum one at 1 s^{-1} (Fig. 4a, Table 1), while the stress-strain curves for 30 different realizations are barely distinguishable at 1×10^7 s^{-1} (Fig. 4b). It should be emphasized that the strength scatter is dependent strongly on the level of microstructural disorder that is arbitrarily selected to

be rather pronounced in this study: $\alpha = 0.02$ and $\beta = 0.5$. The increase of the microstructural-disorder parameters reduces the data scatter.

Table 1 presents statistics of the dynamic tensile strength describing these qualitative observations. The increase of the dynamic strength over the seven decades of the strain rate is sixteen times[2]. This general trend is well documented for wide range of engineering materials over the past three decades (Klopp et al., 1985; Zhou and Clifton, 1997; Grady, 1998; Sarva and Nemat-Nasser, 2001; Brara et al., 2001). Additionally, the strength increase is qualitatively similar to the strain-rate dependence of both the upper yield strength (calculated for ductile metals by Gillis (Gilman, 1969)) and the failure stress (modeled for ceramics under compression by Nemat-Nasser and Deng, 1994). It is interesting to note that, although the simplicity of the present model makes any quantitative comparison with experimental results a tentative undertaking, the ratio of the dynamic strength and the modulus of elasticity for the high loading rates $\sigma_m / E_0 \approx 1 \times 10^{-3}$ agree well with the ratio of the spall strength[3] and the modulus of elasticity $\sigma_{sp} / E_0 \approx 1/1500 \div 1/500$ compiled by Grady (1998) for several ceramic materials.

[2] The strength increase is dependent strongly on the level of microstructural disorder and the degree of nonlinearity of the link force under compression. The increase of α and β reduces the ratio between the upper- and lower-strength asymptotes, and so does the reduction of the repulsive wall steepness (see Mastilovic and Krajcinovic, 1999).

[3] The dynamic tensile strength under uniaxial strain.

The most important observation that can be made from Table 1 is the ordering effect of the kinetic energy on structure-sensitive properties, such as the dynamic strength. Specifically, the standard deviation of the dynamic strength, as a measure of the data scatter, reduces almost by an order of magnitude from 1 s^{-1} to 1×10^{7} s^{-1}. This observation suggests that level of influence of the flaw structure of the brittle material on its dynamic behavior depends on the loading rate. In other words, the ordering effect of kinetic energy implies reduction of the microstructural sensitivity with the increase of the loading rate.

The stress-strain curves at 13 loading rates for the same statistical realization (i.e., for the same pseudo-random number generator seed) are plotted in Fig. 5; the corresponding dynamic tensile strengths are presented in Fig. 6. (The modulus of elasticity difference, evident in Fig. 5, is an artifact of the extreme geometrical and, to a lesser extent, structural disorder.) It is obvious from Fig. 5b that the dynamic strength reaches an upper limit for $\dot{\varepsilon} \approx 1\times10^{7}\ s^{-1}$. Indicatively, the ultimate strength ($\sigma_m / E_0 = 1\times10^{-3}$) corresponds to the macro-strain of 0.1% that is identical to the failure micro-strain (i.e., the critical link extension, $\varepsilon_{cr} = 0.1\%$). Obviously, the more appropriate choice of the critical link extension (i.e., $\varepsilon_{cr} > 0.1\%$) would result in increase of failure macro-strains.

The scatter of the strength data for the five loading rates, presented in Table 1, is depicted by rectangular boxes in Fig. 6. The scatter box for $\dot{\varepsilon} = 1\times10^{7}\ s^{-1}$ is transformed into a horizontal dash, which is indicative of the substantial reduction of the dynamic-strength scatter at the high loading rates. This suggests that the theoretical strength, defining the upper strength asymptote, is a deterministic property defined primarily by the chemical bonding and relatively insensitive to the subtle features of the material texture.

The bilinear log-log plot presented in Fig. 6b is obtained by mapping the simulation data from Fig. 6a. The first linear region, corresponding to data points preceding the upper plateau (the upper strength asymptote), is described by the following scaling relationship between the uniaxial dynamic strength and the strain rate

$$\sigma_m \propto \dot{\varepsilon}^{\zeta} \tag{1}$$

where $\zeta = \Phi - \xi$, and Φ and ξ are parameters defined in Fig. 6b.

The lattice simulations, for different physical realizations of the microstructural statistics defined in Section 2.1, resulting in Fig. 6, suggest that

$$\sigma_m \propto \dot{\varepsilon}^{1/6} \tag{2}$$

The lower plateau (the quasi-static strength asymptote) is just hinted in Fig. 6a since the quasi-static simulations are beyond the scope of this study. This asymptote is, obviously, parallel to the upper strength asymptote (i.e., $\Phi = \xi = 1$). It should be noticed that the relatively small value of the scaling exponent, $\zeta = 1/6$, is due to the rather protracted region of the rapid strength increase (the transient region). On the other hand, the diminishing effect of the microstructural subtleties on the dynamic strength would imply that $\zeta \to 0$ with increase of the microstructural order (within the present model nomenclature, as $\alpha \to 1$ and $\beta \to 1$).

In a more sophisticated spall-strength analysis of Grady and co-workers (presented in Grady, 1995) a distinction is made between two strain-rate ranges. In the first range

(which extends roughly from quasi-static to moderate loading rates) the spall strength is governed by the critical flaw size. In the second range the critical flaw, due to the loading rate increase (approximately $\dot{\varepsilon} \geq 10^5\ s^{-1}$), "no longer responds in a quasi-static manner to the time-varying stress field" (Grady, 1995), consequently, spall strengths are predicted to become dependent on the loading strain rate and independent of the critical flaw size:

$$\sigma_{sp} = \left(\mathrm{A}\, \frac{\dot{\varepsilon}}{\dot{\varepsilon}_o} \right)^{1/3} \sigma_{th} \tag{3}$$

In Eq. (3), $\dot{\varepsilon}_o$ is the critical strain rate and σ_{th} is the theoretical strength (see Grady, 1995, for details). If the surface energy, which must be overcome by the elastic deformation energy to initiate fracture growth, is denoted by γ; the excess surface energy parameter $\mathrm{A} = \gamma / \gamma_{th} > 1$ defines contribution of additional dissipation through plasticity and comminution processes on the theoretical surface energy γ_{th}. Grady stipulates that A can be expected to depend on the strain rate. Assuming that the scaling relationship (1) holds for the spall strength, the scaling relationship between the excess surface energy parameter and the strain rate may be suggested in the following form:

$$\mathrm{A} \propto \dot{\varepsilon}^{3\zeta - 1} \tag{4}$$

For example, $\mathrm{A} \propto \dot{\varepsilon}^{-1/2}$, for simulation results represented by relationship (2).

3.2 Damage evolution

The micro-mechanisms of damage evolution observed in the present simulations are the nucleation, propagation, and clustering of microcracks. As the damage evolves the effective macro-stiffness reduces. The rate of the effective-stiffness reduction, the level of the effective stiffness at failure, and the primacy of a particular damage micro-mechanism, are closely connected characteristics of material behavior that are strongly strain-rate dependent.

Two typical damage patterns are presented in Fig. 7. The snapshot in Fig. 7a is obtained from the $\dot{\varepsilon} = 1 \times 10^4 \ s^{-1}$ simulation. The damage pattern in Fig 7b is obtained from the $\dot{\varepsilon} = 1 \times 10^7 \ s^{-1}$ simulation, which practically corresponds to the strength saturation at the upper strength asymptote.

The damage patterns at high loading rates (represented by Fig. 7b) are characterized by a uniform microcrack distribution. The preferable microcrack surface orientation is, as expected, perpendicular to the loading direction. The typical microcrack cluster, at the onset of softening phase, consists of only a couple of broken links (e.g., from one to five), which are uniformly distributed throughout the sample. At that time, the characteristic distance between the clusters is commensurate with their size. The final sample rupture is preceded by a relatively protracted softening phase (Fig. 5b). The sample's load-carrying capacity is reduced to zero ($\varepsilon = 0$ and $\dot{\sigma} < 0$) after a period of time that is a couple of times longer than the duration of the hardening phase. (This inelastic behavior is a contrast to the moderate-strain-rate failure that is characterized by almost complete absence of the softening phase (Fig. 4a).) The fraction of broken links at the time of the

sample failure asymptotically approaches the total fraction of links that are loaded in tension; this, within the limitations of the present model, resembles comminution of the material. The kinetic energy of the sample, at this loading rate level, exceeds its potential energy by a few orders of magnitude. The snapshot presented in Fig. 7b and the observation that the externally supplied energy overwhelms the cohesive energy of the material, suggest that: (i) the dominant mechanism of damage evolution is the microcrack nucleation resulting in a comminution, and (ii) the role of cooperative phenomena in the damage evolution is unimportant.

The change in the $\dot{\varepsilon} = 1 \times 10^4 \ s^{-1}$ damage pattern (Fig. 7a) compared to the high strain-rate results presented in Fig. 7b can be interpreted by an increasing influence of the microstructural disorder (the initial and induced flaw microstructure of the material) on the macroscopic material response. The microcrack clouds, which dominate the damage patterns at the softening-phase end of the $\dot{\varepsilon} = 1 \times 10^4 \ s^{-1}$ simulation, consist of a large number of broken links. The clusters are elongated predominantly perpendicular to the loading direction; their length, in that direction, is typically between $(30 \div 40)\, l_c$. The clusters are uniformly distributed throughout the sample. The mutual distance between the largest clusters is commensurate with their size. This cluster map suggests the typical fragment size, which is larger substantially that the one corresponding to the $\dot{\varepsilon} = 1 \times 10^7 \ s^{-1}$ simulation. This observation agrees with the prediction by Grady and Kipp (Grady, 1982) regarding the fragment size dependence on the strain rate (see also, Sarva and Nemat-Nasser, 2001). With the further reduction of the loading rate the number and size of, and mutual distance between, the dominant microcrack clouds reduces as well, implying further reduction of the fragment size. For example, for the

$\dot{\varepsilon} = 1 \times 10^3 \ s^{-1}$ simulation, the size of the dominant clusters is somewhat smaller for the damage patterns at the end of the narrow softening-phase (at the onset of failure) from their $\dot{\varepsilon} = 1 \times 10^4 \ s^{-1}$ counterparts, but the mutual distance between the clusters is increased notably.

An insight into the microscale damage dynamics leading to the damage patterns observed for $\dot{\varepsilon} = 1 \times 10^3 \ s^{-1}$ and $\dot{\varepsilon} = 1 \times 10^4 \ s^{-1}$ is offered by the energy time-histories, such as those of Fig. 8. In both cases, the kinetic energy and the potential (deformation) energy are, roughly, of the same order of magnitude; but the total (externally supplied) energy is higher for the higher loading rate. As a consequence, the initial phase of relatively uniform microcrack nucleation, characterizing the hardening phase of material's response, is followed by a more extended damage localization for the higher loading rate compared to the lower one. Since there is no enough energy for the widespread clustering observed at the $\dot{\varepsilon} = 1 \times 10^4 \ s^{-1}$ simulation, the $\dot{\varepsilon} = 1 \times 10^3 \ s^{-1}$ clustering occur only at the most favorable locations while comparably large number microcracks remain isolated and inactive. Consequently, the softening phase of the stress-strain curve corresponding to the $\dot{\varepsilon} = 1 \times 10^4 \ s^{-1}$ simulation is more pronounced than the one for the $\dot{\varepsilon} = 1 \times 10^3 \ s^{-1}$ simulation (Fig. 5a). The cooperative phenomena (reflected in the growth and coalescence of microcrack clouds) plays an essential role in the fracture process and the final sample-disintegration mode. In both cases, the kinetic energy and the potential (deformation) energy are of the same order of magnitude, but for the lower strain rate simulation the constant kinetic energy is relatively early exceeded by the potential energy (the quadratic parabola). In other words, the externally supplied energy is converted primarily into the sample potential energy.

With further reduction of the input energy (that is, further decrease of the loading rate) the dynamic response of the material is distinguished by the localization of microcracks in only a couple of clusters; in the quasi-static case – in a single dominant cluster (Mastilovic and Krajcinovic, 1999). The quasi-static tensile strength is, thus, controlled by a critical weak link (flaw, defect), and the failure macro-strain is an order of magnitude smaller than the critical micro-strain ($\varepsilon_{cr} = 0.1\%$). This marks transition from deterministic to random damage evolution patterns.

Finally, the two phases of the damage accumulation, hardening and softening, are reflections of the primary mechanism of damage growth.

In the hardening phase the specimen is statistically homogeneous regardless of the loading rate. The nucleation of microcracks at weak links (and hot spots, in general) is the paramount mechanism of damage evolution; the distances among microcracks are unlikely to be small, and the amplifying interaction effect of microcracks is insignificant.

In the softening phase the specimen is, with notable exception of the upper-plateau loading rates, random heterogeneous. The damage process depends on the formation and interaction of large clusters, which is driven by the loading energy.

Signatures of the phase transition, close to the peak of the stress-strain curve, are the damage localization and the reduction of the effective stiffness.

4. Summary

The objective of this work is to investigate universal trends in which the disorder and strain rate influence dynamic behavior of the idealized brittle material, by performing

repeated lattice simulations for different physical realizations of the microstructural statistics. The dynamic simulations of the uniaxial tension test, $\dot{\varepsilon} \in \left[0.1\ s^{-1}, 1\times10^{8}\ s^{-1}\right]$, are performed under practically identical stress conditions. The results reveal the ordering effect of the kinetic energy on the dynamic response of the idealized brittle material reflected by transition from the random to deterministic behavior. This transition is evident in the reduction of the strength dispersion (Fig. 9) and damage evolution patterns. The ordering effect of kinetic energy may be attributed to the diminishing flaw-sensitivity of brittle materials with the loading-rate increase. The flaw structure of the material (inherent and induced) is crucial in determining the dynamic tensile strength at low loading rates. With the loading-rate increase, the dynamic strength is becoming increasingly a deterministic property defined by the chemical bonding.

At high loading rates, the external energy overwhelms the cohesive energy of the material resulting in the pulverization. The corresponding uniformity of damage evolution patterns indicates an absence of the cooperative phenomena in opposition to the clustering of microcracks into microcrack clouds characteristic of the medium loading range. The evolution of the microcrack clouds may represent the dominant toughening mechanism in brittle materials not susceptible to dislocation activities. The effect of this process is reflected by the pronounced inelastic behavior not only in the softening but also in the hardening phase. These observations are reminiscent of Anderson's (1958) conclusions that: (1) localization is impossible in the absence of disorder and (2) the localization range depends on the frequency and energy of electron waves.

References

Allen, M.P., Tildesley, D.J., 1994. Computer Simulation of Liquids. Oxford University Press Inc., Oxford.

Anderson, W., 1958. Absence of Diffusion in Certain Random Lattices. Phys. Rev., 109, 1492-1505.

Brara, A., Camborde, F., Klepaczko, J.R., Mariotti, C., 2001. Experimental and numerical study of concrete at high strain rates in tension. Mech. Mater., 33, 33-45.

Curtin, W.A., Scher, H., 1990. Brittle fracture in disordered materials: a spring network model. J. Mater. Res., 5, 535-553.

Davidge, R.W., Green, T.J., 1968. Strength of two-phase ceramic / glass material. J. Mater. Sci., 3, 629-641.

Espinosa, H.D., Zavattieri, P.D., 2003. A grain level model for the study of failure initiation and evolution in polycrystalline brittle materials. Part I: Theory and numerical implementation. Mech. Mater., 35, 333-364.

Gilman, J.J., 1969. Micromechanics of Flow in Solids. McGrow-Hill, New York.

Grady, D.E., 1982. Local inertial effects in dynamic fragmentation. J. Appl. Phys., 53, 322-325.

Grady, D.E., 1995. Dynamic Properties of Ceramic Materials. SAND94-3266 · UC-704. Sandia National Laboratories, Albuquerque, pp. 26-31.

Grady, D.E., 1998. Shock-wave compression of brittle solids. Mech. Mater., 29, 181-203.

Holian B.L., Grady D.E., 1988. Fragmentation by Molecular Dynamics: The Microscopic "Big Bang." Phys. Rev. Letters, 60 (14), 1355-1358.

Hoover, W.G., 1986. Molecular Dynamics. Springer-Verlag, Berlin.

Jagota A., Bennison S.J., 1994. Spring-Network and Finite-Element Models for Elasticity and Fracture, in: Bardhan, K.K., Chakrabarti, B.K., Hansen, A. (Eds.), Proceedings of a workshop on breakdown and non-linearity in soft condensed matter, Springer-Verlag Lecture Notes in Physics, Berlin, pp. 186-201.

Klopp, R.W., Clifton, R.J., Shawki, T.G., 1985. Pressure-Shear Impact and the Dynamic Viscoplastic Response of Metals. Mech. Mater., 4, 375-385.

Krajcinovic, D., 1996. Damage Mechanics. North-Holland, Amsterdam.

Lawn, B., 1993. Fracture of Brittle Solids. Second Edition. Cambridge University Press, Cambridge.

Mastilovic, S., Krajcinovic, D., 1999. Statistical models of brittle deformation Part II: Computer simulations. Int. J. Plasticity, 15, 427-456.

Mastilovic, S., Krajcinovic D., 1999a. High-velocity expansion of a cavity within a brittle material. J. Mech. Phys. Solids, 47, 557-610.

Nemat-Nasser, S., Deng, H., 1994. Strain-rate effect on brittle failure in compression. Acta Metall. Mater. 42 (3), 1013-1024.

Nicholas, T., Bless, S.J., 1985. High strain rate tension testing, in: Mechanical Testing, Metals Handbook 8. Am. Soc. Metals, Metals Park, pp. 208-214

Sarva, S., Nemat-Nasser, S., 2001. Dynamic compressive strength of silicon carbide under uniaxial compression. Materials Science and Engineering, A317, 140-144.

Straβburger, E., Senf, H., 1995. Experimental Investigation of Wave and Fracture Phenomena in Impacted Ceramics and Glasses, Fraunhofer-Institut Fur Kurzzeitdynamik, Ernst-Mach-Institut, Weil am Rhein, Germany.

Vitek, V., 1996. Pair potentials in atomistic computer simulations, in: Voter, A.F. (Ed.), Interatomic Potentials for Atomistic Simulations, MRS Bulletin, 21 (2), pp. 20-23.

Wiener, J.H., 1983. Statistical Mechanics of Elasticity. J. Willey and Sons, New York.

Zhou, M., Clifton, R.J., 1997. Dynamic Constitutive and Failure Behavior of a Two-Phase Tungsten Composite. J. Appl. Mech., 64, 487-494.

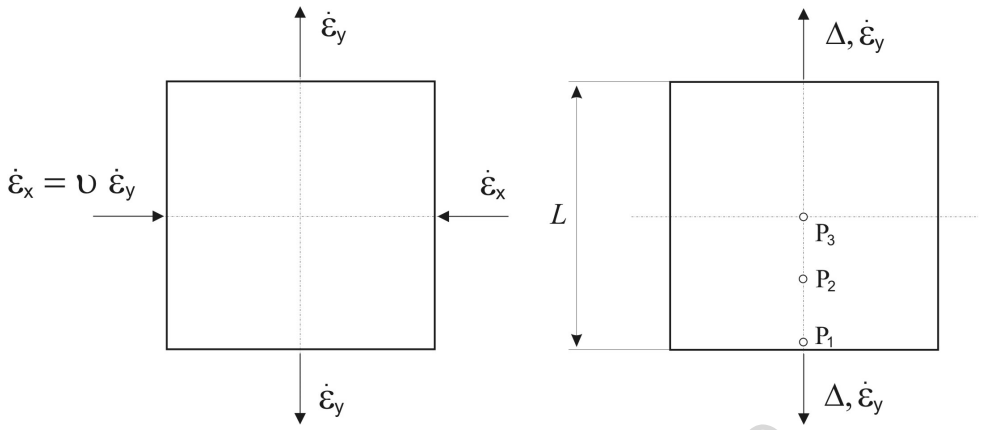

Fig. 1. Schematic representation of the uniaxial tension test setup: (a) application of the initial strain rate field, and (b) displacement-controlled tension.

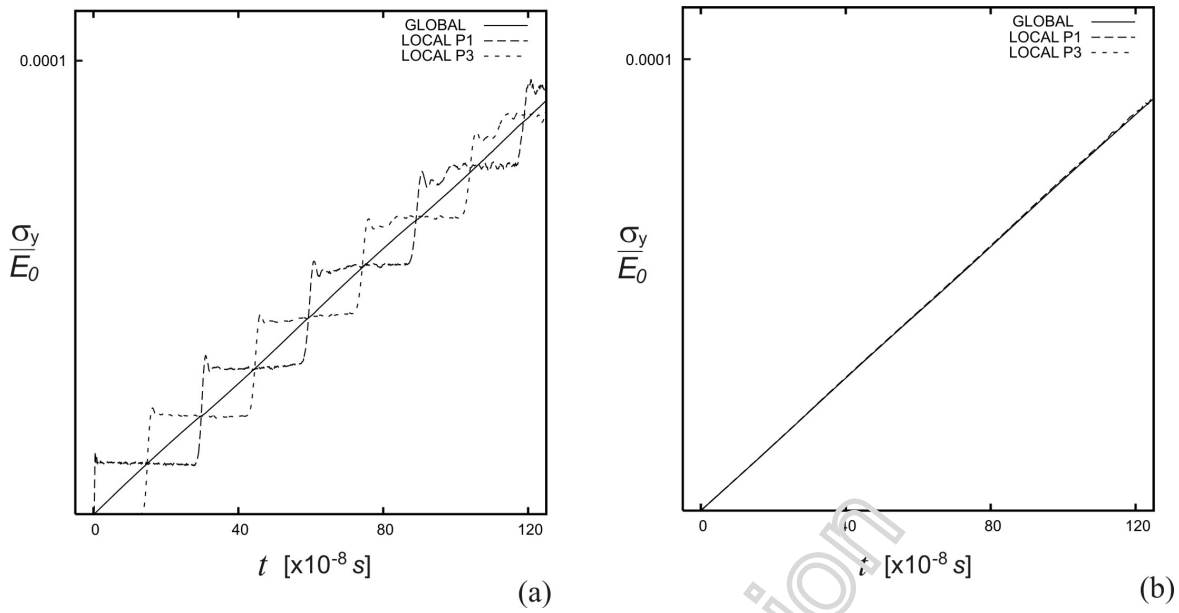

Fig. 2. The effect of initially applied strain-rate fields on transient, local and global (averaged), strain evolution during the uniaxial tension test (100 s^{-1}); (a) without, and (b) with application of the initial strain-rate fields.

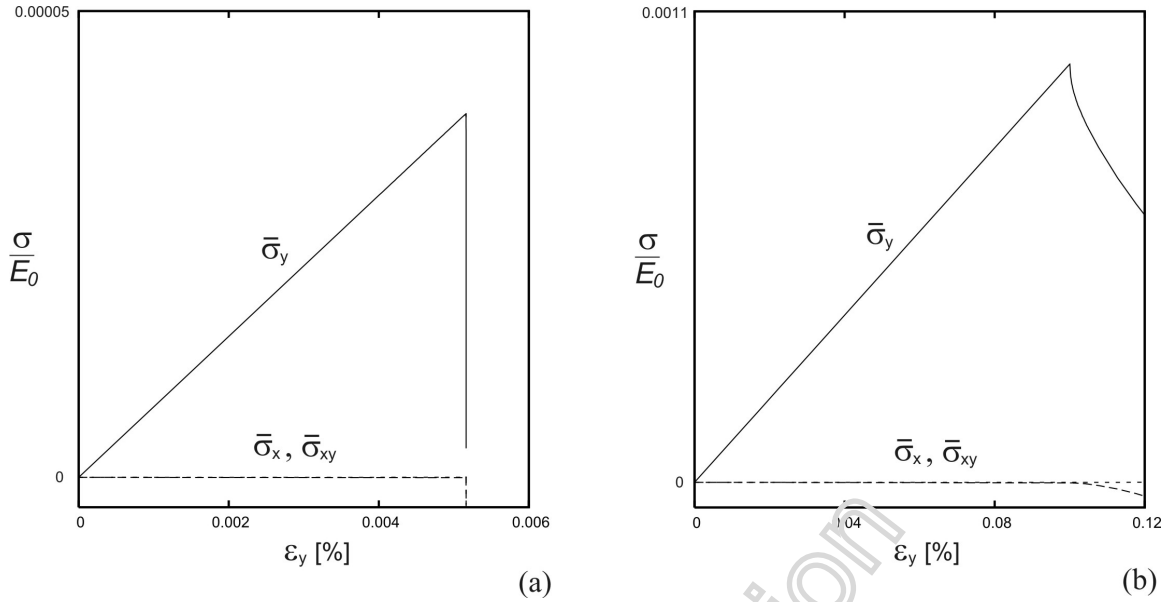

Fig. 3. Stress components vs. longitudinal strain for two widely different strain rates: (a) $0.1\ s^{-1}$, and (b) $1\times10^{8}\ s^{-1}$.

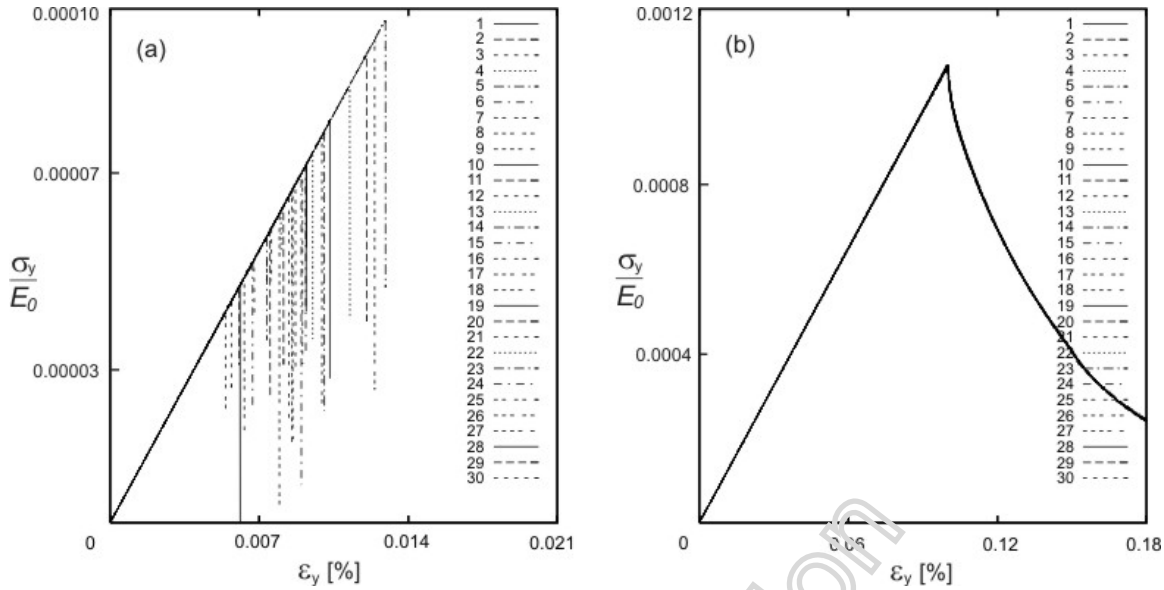

Fig. 4. Normal stress in longitudinal direction plotted vs. normal strain in the same direction for 30 statistical realizations at two different loading rates: (a) 1 s^{-1}, (b) 1×10^{7} s^{-1}.

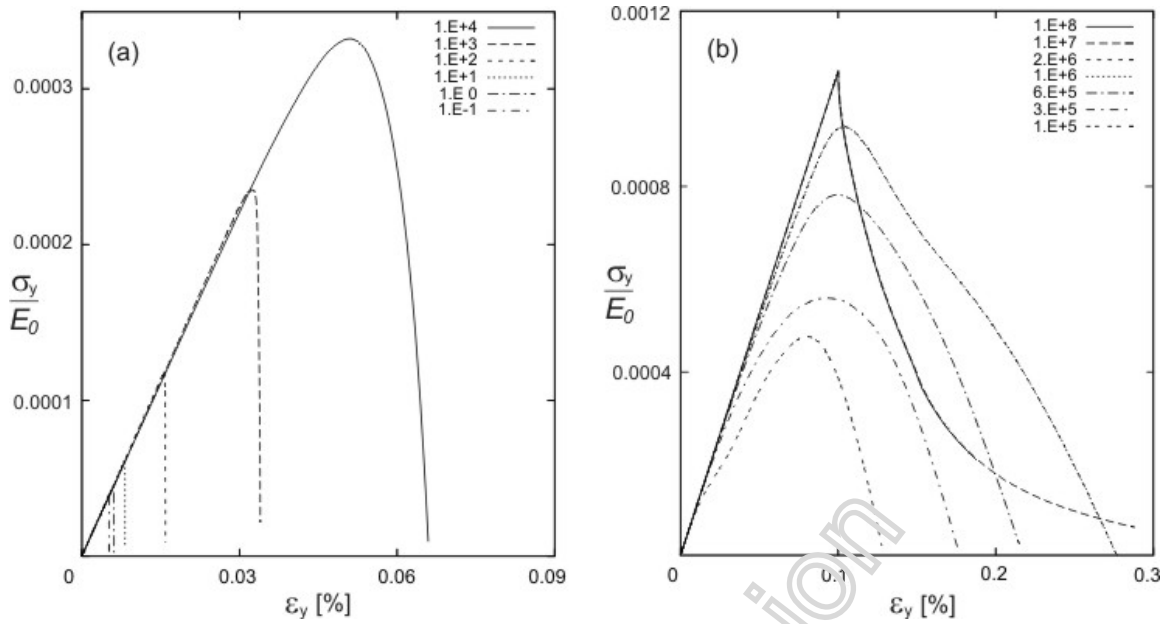

Fig. 5. Normal stress plotted vs. normal strain (in the loading direction) for thirteen different strain rates of loading of the same physical realization of microstructural statistics.

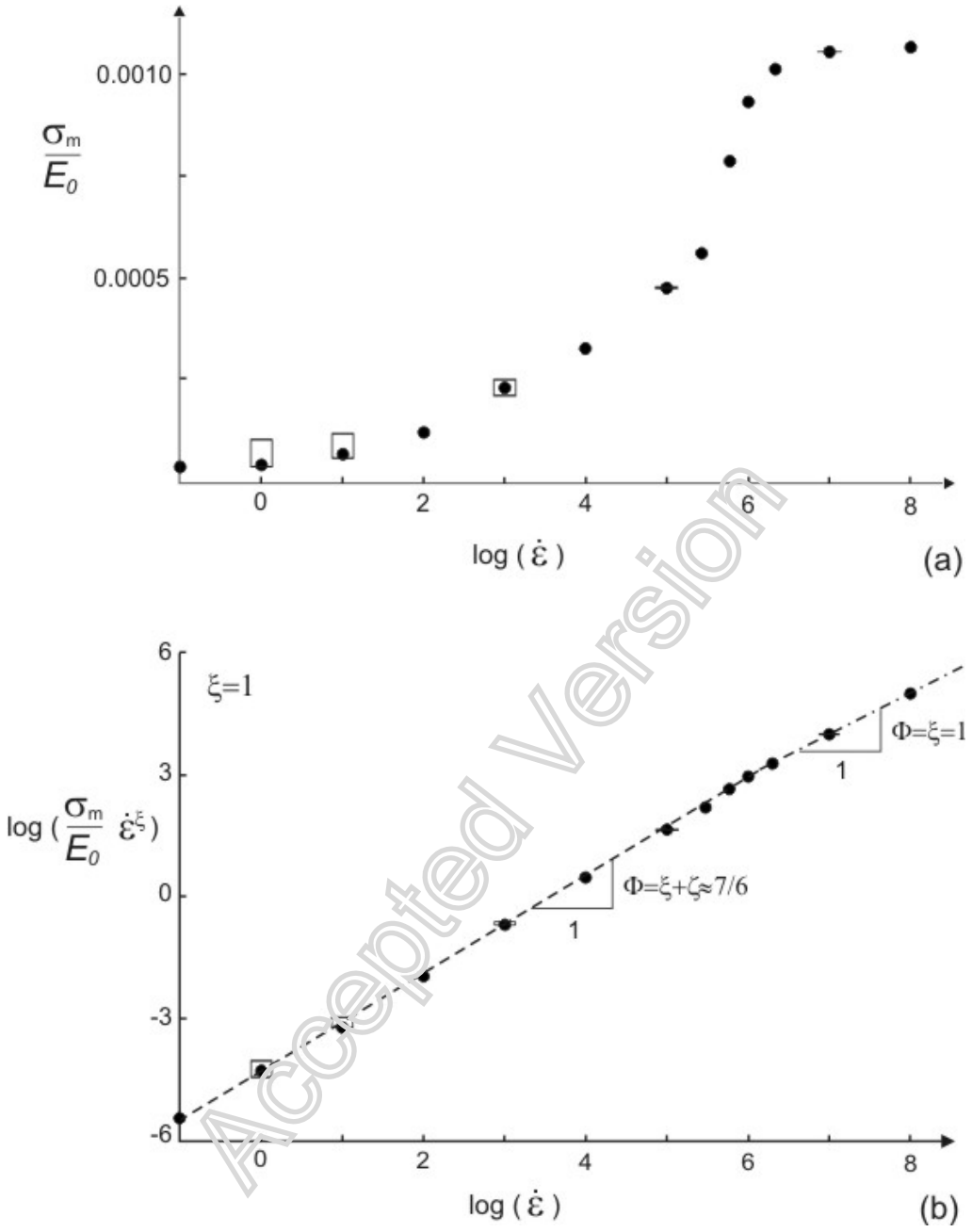

Fig. 6. Dynamic tensile strength vs. strain rate: (a) original plot, (b) scaled plot.

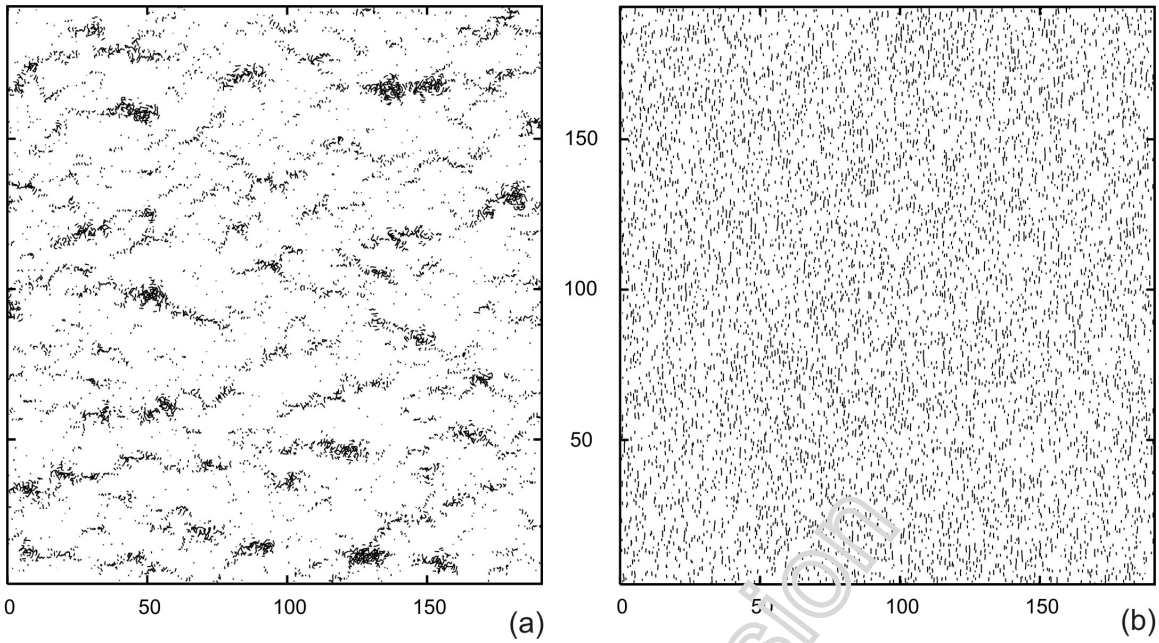

Fig. 7. Damage patterns at two different loading rates: (a) $1\times10^{4}\ s^{-1}$, (b) $1\times10^{7}\ s^{-1}$. Both snapshots are recorded in the softening phase of deformation and correspond to ($t = 65.8\ ns$, $\varepsilon_y = 0.0658\%$) and ($t = 0.104\ ns$, $\varepsilon_y = 0.104\%$), respectively. (Dashes represent broken links.)

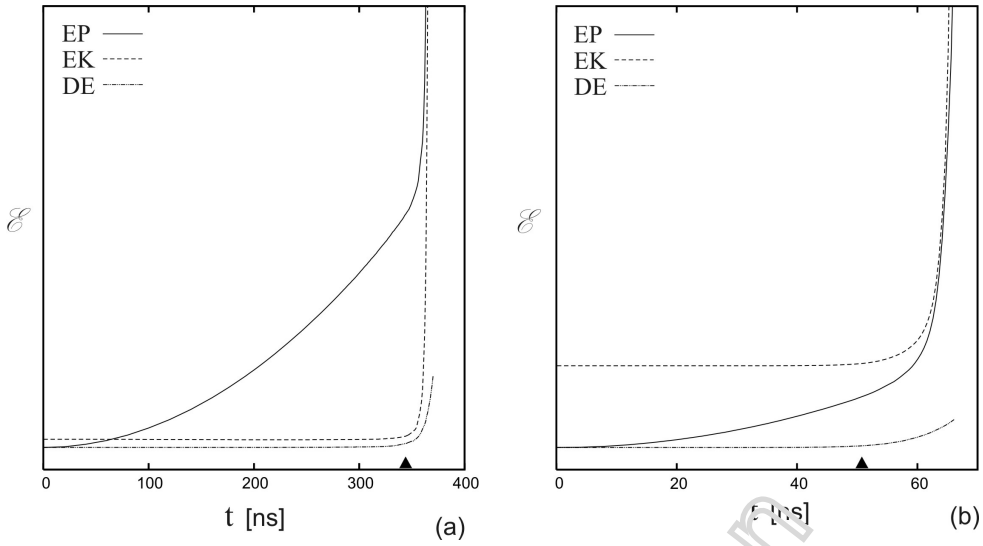

Fig. 8. Schematic energy time-history at two different loading rates: (a) 1×10^{3} s^{-1}, (b) 1×10^{4} s^{-1} characterized by a notable effect of cooperative phenomena (EP, EK, and DE correspond to potential, kinetic, and damage energy, respectively).

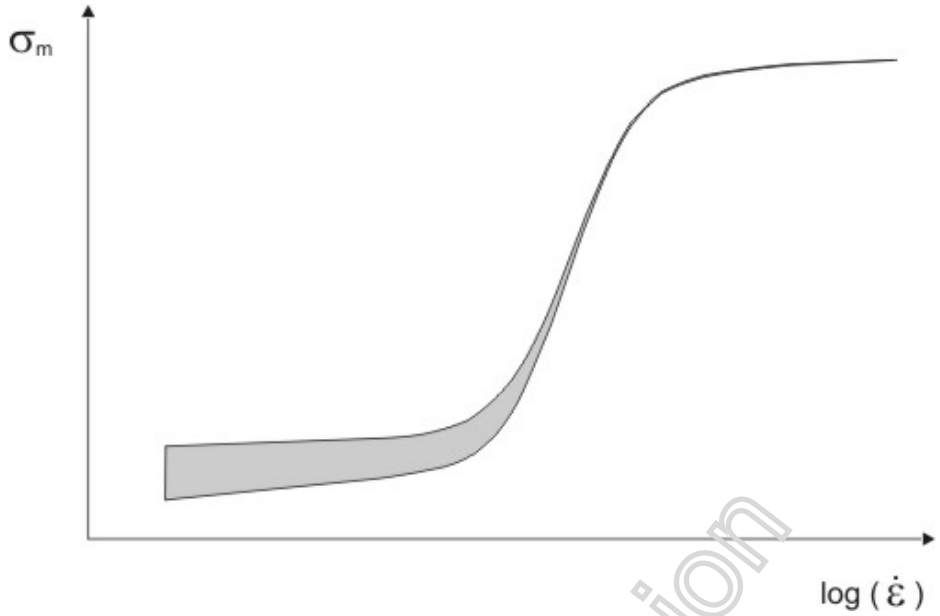

Fig. 9. Schematic representation of the dynamic strength dependence on the strain rate indicating the ordering effect of kinetic energy

Table 1. Statistics of the dynamic tensile strength statistics at four different loading rates

$\dot{\varepsilon}$ [1/s]		1	10	1×10^{3}	1×10^{5}	1×10^{7}
σ_m/E_0 [$\times10^{-3}$]	MEAN	0.0649	0.0887	0.235	0.482	1.07
	STANDARD DEVIATION	0.0147	0.0155	0.0115	0.00209	0.00185
	MAXIMUM	0.0975	0.112	0.252	0.487	1.07
	MINIMUM	0.0409	0.0615	0.204	0.478	1.07
	MAXIMUM / MINIMUM	2.55	1.94	1.32	1.08	1.07